Estimate of the ^{225}Ac Radioactive Isotope Distribution by Means of DOI Compton Imaging in Targeted Alpha Radiotherapy: A Monte Carlo Simulation

Changyeon Yoon

Decommissiong Technology Group, Central Research Institute,
Korea Hydro & Nuclear Power, Dajeon 34101, Korea

Seongmin Jo, Yongho Cho, Nakjeom Kim and Taewoong Lee*

Global Institute of Technology, KEPCO KPS, Naju 58326, Korea

For successful targeted alpha radiotherapy (TAT), verifying the accurate position and distribution of a targeted radiotherapeutic agent in a patient or phantom is important. This paper, describes our investigation of depth-of-interaction (DOI) Compton imaging for the two γ-rays emitted during TAT with the ^{225}Ac radioactive isotope. We optimized the design parameters of the DOI Compton camera, for example, the inter-detector distance, based on the figure of merit (FOM). The performance of DOI Compton imaging for TAT was improved because Doppler broadening and the energy uncertainty are inversely proportional to the radiation energy and the position uncertainty of the depth information is decreased. After the contrast phantom and the resolution phantom had been designed, two reconstruction algorithms, the filtered back-projection (FBP) algorithm and the maximum-likelihood expectation maximization (MLEM) algorithm, were applied to each reconstructed phantom image, and the qualities of the reconstructed images for the two γ-rays (218 keV and 440 keV) were compared. In the quantitative evaluation of the reconstructed images, the MLEM reconstruction algorithm performed better than the FBP algorithm. Based on Monte Carlo simulation studies, the DOI Compton images of the ^{225}Ac radioactive isotope emitting two γ-rays demonstrated the capability of imaging a targeted radiotherapeutic agent in TAT.

I. INTRODUCTION

Due to the short stopping power and the high linear energy transfer (LET) of alpha particles, a concentrated radiation dose can be administered to a tumor while exposure to adjacent normal tissues and critical organs is minimized. Therefore, targeted alpha therapy (TAT) using α-emitting radionuclides is a promising approach to selectively treating cancers [1–4]. Most α-emitting radionuclides produce various daughter radionuclides through their decay and emit various radiation particles, including high-energy γ-rays. Recently, the ^{225}Ac radionuclide with a relatively long half-life ($t_{1/2} = 10$ d) has been utilized for TAT [5–8]. ^{225}Ac decays to stable ^{209}Bi through two β- and four α- decays, and two γ-rays are emitted via the alpha decay

of its daughter nuclides ^{221}Fr (218 keV) and ^{213}Bi (440 keV) at intensities of 11.6% and 26.1%, respectively [5,9]. Therefore, for *in vivo* monitoring of the α-emitting radionuclide, the distribution and the location of the ^{225}Ac radionuclide in the patient or phantom can be estimated by measuring the γ-rays.

Several imaging systems with a collimator have been used to perform feasibility studies for *in vivo* monitoring of the distribution and the location of radiation sources by using the reconstructed image of high-energy γ-rays [9–11]. However, as the energy of the γ-rays increases, the reconstructed image becomes blurred due to the penetration of radiation and the scattering of the radiation through the collimator. Hence, a Compton camera without a thick collimator has been utilized to reconstruct images of high-energy γ-rays. Moreover, above γ-ray energies of 300 keV, the detection efficiency and the angular resolution of the Compton camera were higher than these previously reported for an imaging system with a
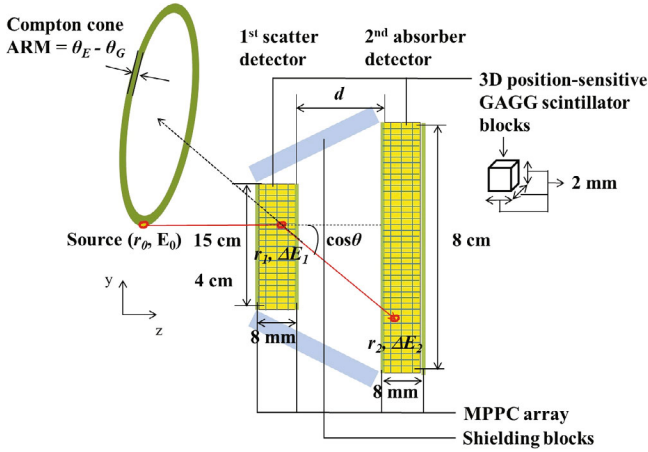
*E-mail: superdapo@kps.co.kr

Fig. 1. Configuration of the DOI Compton camera and the interaction within the detector.

Table 1. X- and γ-ray emissions resulting from the decay of the ^{225}Ac radionuclide. ^{225}Ac emissions with a branching ratio < 1% or an energy < 79 keV are excluded.

Elements	Energy (keV)	Intensity (%/decay)
^{221}Fr	81 (X-ray)	1.45
	218 (γ-ray)	11.4
^{213}Bi	79 (X-ray)	1.99
	440 (γ-ray)	25.9

II. MATERIALS AND METHODS

1. Geometry Design and GATE Simulation of the DOI Compton Camera

The simulation configuration is shown in Fig. 1. If the γ-rays undergo effective Compton scattering followed by absorption, the positions (r_1 and r_2,) and the energies (ΔE_1 and ΔE_2) of the two interactions are acquired by the two detectors, respectively. The Compton cone (r_0 and ΔE_0) can be estimated using the Compton formula [26]; hence, the distribution of the source including the ^{225}Ac radionuclide in the phantom can be inferred from the γ-ray distribution. The γ-rays and the X-rays from the ^{225}Ac radionuclide are shown in Table 1 [9,11]. Because the γ-rays and the X-rays with low energy cannot provide images representing the distribution of the Compton cone, only 218 (11.4%) and 440 keV (25.9%) are used to reconstruct the Compton images. In all the simulation studies, the primary sources are γ-rays, whose main energy peaks are located at 218 keV and 440 keV. The distance between the surface of the scatter detector and the source was set to 15 cm. All simulation studies were performed by using the Geant4 application for tomographic emission (GATE 7.0). The physics of the γ-rays was modeled by applying Penelope in the Geant4 toolkit [27,28]. In optimization of geometry study, the point source activity was set to 0.37 MBq, and the simulation times were 10 min.

In the simulation study, we modeled cerium-doped gadolinium-aluminum-gallium garnet (GAGG) crystals developed by Kataoka *et al.* [25]. The Compton camera of the Si-based semiconductor provides an imaging resolution with little loss of detection efficiency for low-energy γ-rays [28]. However, the application of GAGG blocks is ideal to build blocks for assembling DOI detector arrays, which can provide a larger effective area of the scatter detector at a comparatively low production cost compared to that for Si-based semiconductors. The DOI Compton camera was constructed with two GAGG detector block arrays. The sizes of the scatter and the absorber detectors were $40 \times 40 \times 8$ mm^3 and $80 \times 80 \times 8$ mm^3, respectively. Each voxel had dimensions of $2 \times 2 \times 2$ mm^3. If the distortion of the reconstructed

collimator [12]. The quality of the Compton images is improved at high energy because the Doppler broadening and the energy uncertainty are inversely proportional to the radiation energy [13,14]. These advantages facilitate the application of Compton imaging in proton therapy [15,16], boron neutron capture therapy (BNCT) [17, 18], and nuclear medicine [19–22]. However, the conventional Compton camera utilizes only position and energy information from one layer for each detector module, which limits the position resolution in the depth direction (z-direction). In recent years, 3D position-sensitive scintillator detectors that measure the depth of interactions (DOIs) were developed [23,24] and used for Compton cameras. When the distance between the scatter and the absorber detector is shorter, the Compton imaging using a DOI scintillator detector has demonstrated better performance than conventional Compton imaging [25]. In particular, the angular resolution of the reconstructed image was improved because the position information was precisely calculated, so the position uncertainty of the depth information was decreased [25]. In this study, we used a DOI Compton camera based on a cerium-doped gadolinium-aluminum-gallium garnet (GAGG) scintillator to measure and reconstruct images for the positions and the distributions of the two γ-rays emitted by the ^{225}Ac radionuclide inserted into a phantom. To maximize the performance of the reconstructed images, we optimized the inter-detector distance of the DOI Compton camera. We then applied various Compton reconstruction algorithms and quantitatively evaluated the performance. Moreover, to evaluate the performance of Compton imaging of the ^{225}Ac radionuclide, we used various phantoms. Monte Carlo simulation studies have shown the validity of *in vivo* monitoring using the reconstructed Compton images of the ^{225}Ac radionuclide in TAT.

Compton images is to be minimized, uniform Compton angles should be obtained. Hence, the size of the absorber detector was set at twice the size of the scatter detector.

In Compton imaging, the correct sequence is defined by γ-rays that are scattered from the scatter detector and absorbed by the absorber detector (1st scatter detector - 2nd absorber detector). Moreover, to reduce the random coincidence rate such as the incorrect sequence (2nd absorber detector-1st scatter detector), we shielded the detectors with 50-mm-thick lead plates [21]. The effect of a $BaSO_4$ reflector (0.2-mm thick) in reducing the position uncertainty caused by the spread of the light was not considered because DOI information such as the precise interaction position was obtained in the GATE simulation. Both detectors were coupled to multi-pixel photon counters (MPPCs), and the depth of interaction was calculated based on the ratio of the pulse heights from the tops and the bottoms of the MPPCs [23, 24]. High-quality reconstructed Compton images are to be obtained, the inter-detector distance (d) needs to be optimized in terms of the figure of merit (FOM); hence, only the detection efficiency and the angular resolution measure (ARM) of the reconstructed images were considered:

$$\text{Figure of merit (FOM)} = \frac{\text{Detection efficiency}}{\text{FWHM}^3} \times 10^{10} . \tag{1}$$

The ratio of the number of effective counts used for image reconstruction to the total number of counts of the source activity is the detection efficiency. The ARM is the angular resolution of the detector configuration, which is calculated as the difference between the scattering angles of geometrical information (θ_g) and energy information (θ_e). Hence, the angular resolution can be expressed by using the full width at half maximum (FWHM) of the ARM. The optimization of inter-detector distance of the DOI Compton camera is discussed in subsection of Sec. III.

2. Performance Evaluation of Compton Imaging

Effective Compton events are defined as γ-rays undergoing Compton scattering in the 1st detector and full absorption in the 2nd detector. The energy resolutions of the GAGG detector are 17.4% at 218 keV and 12.2% at 440 keV. The appropriate energy windows for the keV and 440 keV are 218 $\pm$ 37 keV and 440 $\pm$ 53 keV, respectively. After the preferential extraction of effective Compton events by using energy windows, the correct interaction sequence is determined based on a comparison of energies deposited in the detectors. If the energy of the incident γ-ray is higher than 400 keV, a higher energy is accumulated in the 1st detector. In contrast,
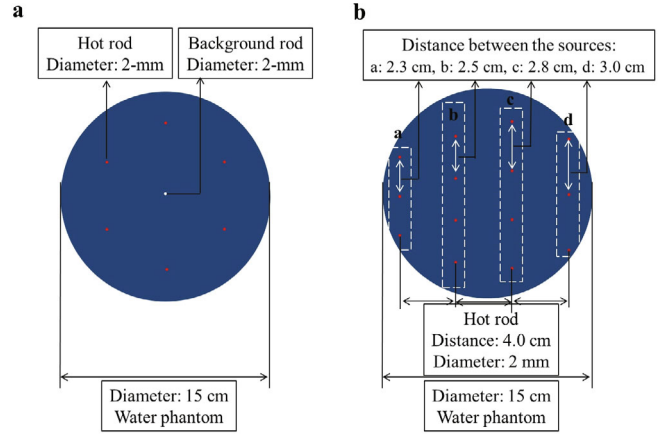

Fig. 2. Simulation phantoms in GATE: a) contrast phantom and (b) resolution phantom.

if the energy of the γ-ray is lower than 400 keV, a lower energy will be deposited in the 1st detector. Effective Compton events are extracted through the fraction of interactions that deposit higher energy. Therefore, the higher number of counts for effective Compton events, which are determined based on the energy window and the correct interaction sequence, guarantees a better performance for the reconstructed images.

A contrast phantom with various source activities per unit volume, was used for the performance evaluation of Compton imaging. As shown in Fig. 2(a), a cylindrical contrast phantom with a radius of 7.5 cm and a height of 2 cm was composed of six hot rods. The diameter and the height of all rods were 2 mm and 2 cm, respectively. The source activities per unit volume were from 3 MBq to 8 MBq, in steps of 1 MBq. The average pixel value of each rod and the effective counts in the reconstructed images were calculated for each rod by using regions of interest (ROIs) with diameters that were 90% of the physical diameter of the rod. The contrast-to-noise ratio (CNR) was defined as C_s/N_s, which C_s is the contrast value for each rod, and N_s, which is the variability between the ROI mean value in each rod, is the noise parameter for each rod [10].

A resolution phantom was utilized to estimate the minimum distance to differentiate the sources. The cylindrical resolution phantom, which had a diameter of 15 cm and a height of 2 cm, consisted of hot rods with 2-mm diameters. The distance between the hot rods positioned in four different segments were 2.3 cm, 2.5 cm, 2.8 cm, and 3.0 cm, as shown in Fig. 2(b).

We used two image reconstruction algorithms to evaluate the performance of Compton imaging. Firstly, to evaluate the Compton imaging in real time, we used the filtered back-projection (FBP) algorithm, which performs calculations event-by-event. The FBP algorithm was proposed and derived by Parra [26]. Because the blurring caused by the simple back-projection (SBP) algorithm was minimized in the reconstructed image,
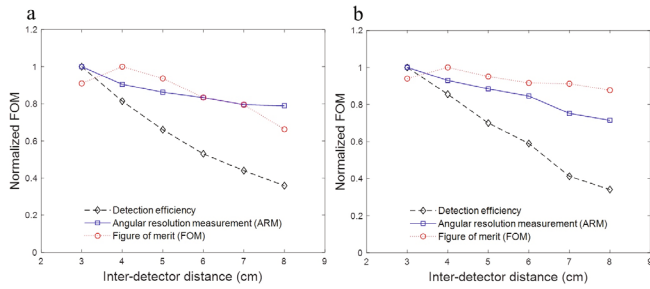
Fig. 3. Performance evaluation for various inter-detector distances using the detection efficiency, angular resolution measurement (ARM), and figure of merit (FOM) for a point source: (a) 218 keV and (b) 440 keV.

Compton imaging using the FBP algorithm provides a higher resolution image than that using the SBP doses [29]. Secondly, the maximum likelihood expectation and the maximization (MLEM) method, which utilized the expectation maximization (EM) algorithm to find the maximum likelihood (ML), was applied to Compton imaging [30]. The EM algorithm for radiation measurements was derived by Lange and Carson [31]. Although the MLEM method, which collects data and updates the image iteratively, is not a real-time reconstruction method, the results from previous studies showed that the Compton image reconstructed by using the MLEM was better than that of the images reconstructed by using SBP and the FBP algorithms [29]. The optimized n-values and the number of iterations for the FBP and the MLEM reconstruction algorithms were set to 30. The performances of the reconstruction algorithm using various phantoms are discussed in subsections 1 and 2 of Sec. III.

III. RESULTS

1. Optimization of the Inter-Detector Distance

Optimization of the inter-detector of DOI Compton camera distance was performed for the 218-keV and the 440-keV γ-ray energies emitted from the ^{225}Ac radionuclide. As shown in Fig. 3, because the angular resolution for the Compton camera is decided by the detector pixel divided by the inter-detector distance, the performance of the ARM improved with increasing inter-detector distances. In contrast, the performance of the detection efficiency decreased because the probability of radiation detection is inversely proportional to the inter-detector distance. The optimization of the inter-detector distance is determined using the FOM considering both these factors. The FOM reached its maximum value when the inter-detector distance was 4 cm. Hence, the optimum inter-detector distance was set to 4 cm to achieve the best performance of the DOI Compton camera. Table 2
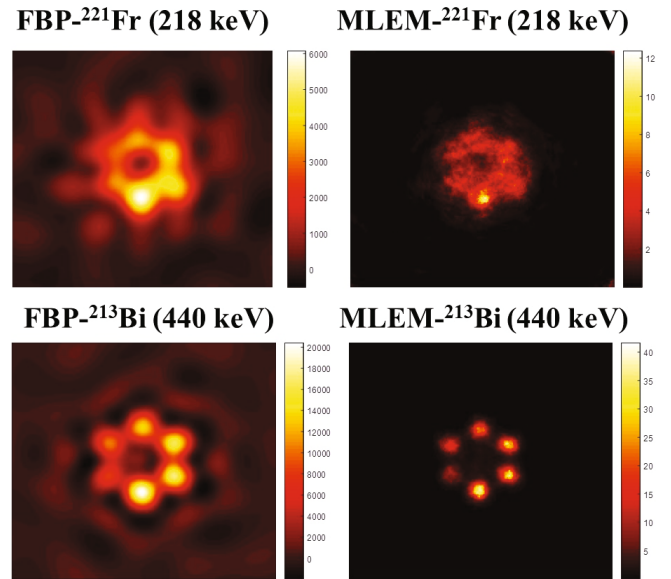

Fig. 4. ^{221}Fr (218 keV) and ^{213}Bi (440 keV) images of the contrast phantom acquired using both the FBP (n-value = 30) and the MLEM (iteration = 30) algorithms.
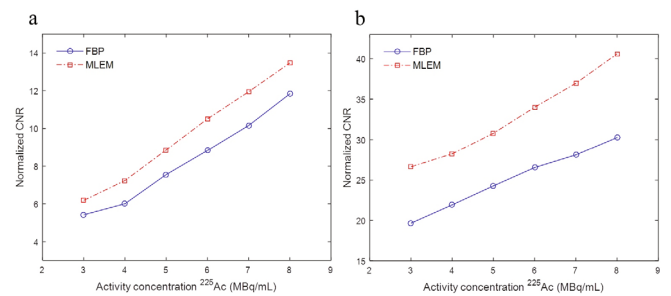

Fig. 5. Evaluation of the contrast-to-noise ratios (CNRs) from the contrast phantom images: (a) ^{221}Fr (218 keV) and (b) ^{213}Bi (440 keV).

shows the detection efficiency and the ARM at an optimized inter-detector distance of 4 cm for a point source.

2. Performance Evaluation of DOI Compton Imaging for the ^{225}Ac Radionuclide

The contrast-to-noise ratios (CNRs) were evaluated and compared after image reconstruction using the FBP and MLEM algorithms. The images reconstructed using the FBP and the MLEM algorithms at 218 keV and 440 keV are shown in Fig. 4. Because the energy uncertainty and the Doppler broadening of the DOI Compton camera for 440 keV was smaller than those for 218 keV, the quality of the reconstructed image for 440 keV was improved. The CNRs using FBP and MLEM for 218 and 440 keV are shown in Fig. 5. The performance of the CNR improved when the source activities per unit

Table 2. Performance of the DOI Compton camera using a point source.

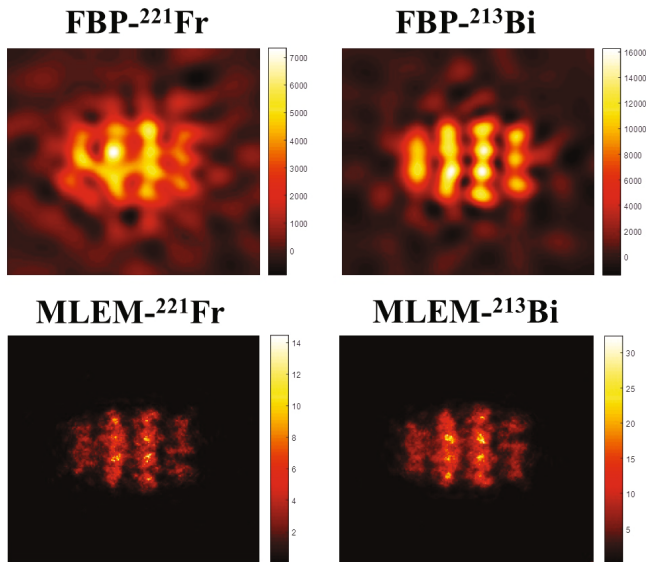| Elements	Energy (keV)	Detection efficiency	Angular resolution measure (ARM)
^{221}Fr	218	5.6×10^{-5}	16.2
^{213}Bi	440	4.6×10^{-5}	10.8

Fig. 6. ^{221}Fr (218 keV) and ^{213}Bi (440 keV) images of the resolution phantom acquired using the FBP (n-value = 30) and the MLEM (iteration = 30) algorithms.

Fig. 7. Evaluation of the y-profile from each rod in the resolution of the phantom image for ^{221}Fr (218 keV). Profiles from the FBP images are shown on blue solid lines, and profiles from the MLEM images are shown on red dashed lines.

Fig. 8. Evaluation of the y-profile from each rod in the resolution of the phantom image for ^{213}Bi (440 keV). Profiles from the FBP images are shown on blue solid lines, and profiles from the MLEM images are shown on red dashed lines.

volume were increased, which was mainly due to the increase in the effective number of Compton counts. As the effective number of Compton counts increased, the value of C_s improved while the value of N_s decreased. Because of the statistical uncertainty of the calculated number of counts having been minimized, the images reconstructed using the MLEM algorithm were sharper and had fewer artifacts than those reconstructed using the FBP algorithm. Therefore, the reconstructed Compton images obtained using the MLEM algorithm had a higher CNR than those obtained using the FBP reconstruction algorithm.

After reconstruction for the resolution phantom by using the FBP and MLEM algorithms, the average FWHM and the relative standard deviation (RSD) were calculated for each rod to evaluate the quality of the reconstructed image. The reconstructed images for 218 keV and 440 keV emitted from the ^{225}Ac radionuclide are shown in Fig. 6. The Compton images reconstructed using the MLEM algorithm exhibited less noise and fewer artifacts than the Compton images reconstructed using the FBP algorithm.

The trends of the reconstructed images were similar to those for the reconstructed images of the contrast phantom. The RSD was defined as the standard deviation of source pixels/mean value of source pixels for each rod
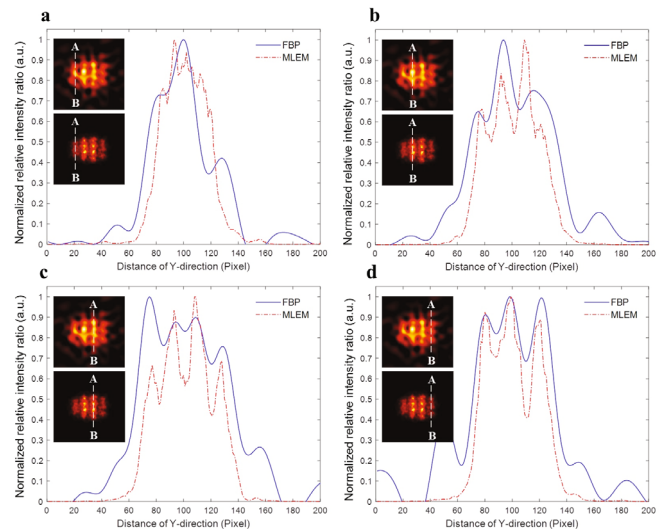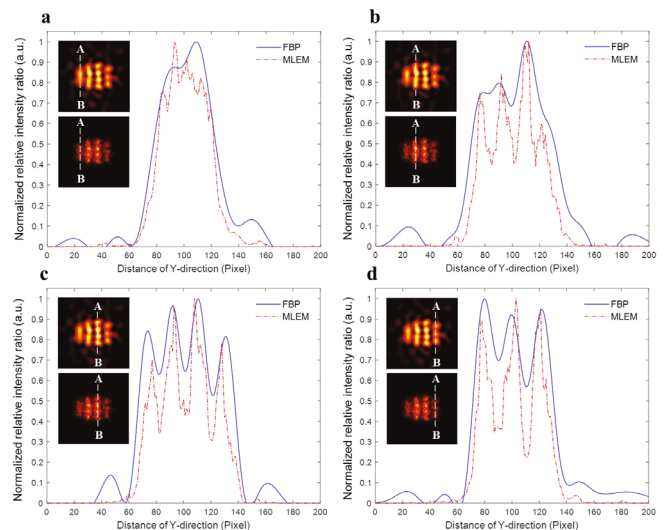
when using ROIs with diameters that were 90% of the FWHM. For the RSD, a lower value indicates that the statistical fluctuation is small and demonstrates better performance. The performances of the MLEM algorithm

Table 3. FWHM and RSD for each size at ^{221}Fr (218 keV) and ^{213}Bi (440 keV) (cf. Fig. 6).

Group (cm)	Reconstruction algorithm	^{221}Fr (218 keV)		^{213}Bi (440 keV)	
		Average FWHM (mm)	Average RSD	Average FWHM (mm)	Average RSD
a	FBP	Not measurable	Not measurable	Not measurable	Not measurable
(2.3)	MLEM	Not measurable	Not measurable	Not measurable	Not measurable
b	FBP	Not measurable	Not measurable	Not measurable	Not measurable
(2.5)	MLEM	7.8	0.25	5.9	0.18
c	FBP	8.4	0.31	6.7	0.21
(2.8)	MLEM	8.1	0.24	7.3	0.14
d	FBP	9.3	0.23	7.8	0.14
(3.0)	MLEM	7.4	0.17	6.4	0.11

Table 4. Confidence interval of the reconstructed image pixel value for the resolution phantom (cf. Fig. 6).

Energy (keV)	Reconstruction algorithm	Average image pixel (source)	Average standard deviation	Confidence interval (μ = average pixel value in the image)	
				95%	99%
218	FBP	4122	1113	$3529 \leq \mu \leq 4715$	$3302 \leq \mu \leq 4942$
	MLEM	11324	2718	$9876 \leq \mu \leq 12772$	$93215 \leq \mu \leq 13326$
440	FBP	11	1.9	$9.9 \leq \mu \leq 12.0$	$9.6 \leq \mu \leq 12.39$
	MLEM	26	3.6	$24.1 \leq \mu \leq 28.0$	$23.3 \leq \mu \leq 28.6$

Table 5. Comparison of actual and the measured distances for sources in the reconstructed ^{221}Fr (218 keV) Compton images (cf. Fig. 7).

Content	a	b	c	d
Original distance between sources (cm)	2.3	2.5	2.8	3.0
Measured distance between sources by using FBP (cm)	Not measurable	Not measurable	3.6	3.8
Measured distance between sources by using MLEM (cm)	Not measurable	2.9	3.4	3.4

Table 6. Comparison of actual and the measured distances for sources in the reconstructed ^{213}Bi (440 keV) Compton images (cf. Fig. 8).

Content	a	b	c	D
Original distance between sources (cm)	2.3	2.5	2.8	3.0
Measured distance between sources by using FBP (cm)	Not measurable	Not measurable	3.4	3.7
Measured distance between sources by using MLEM (cm)	Not measurable	2.8	3.2	3.4

for the FWHM and the RSD were higher than those of the FBP algorithm, as shown in Table 3. Table 4 presents the confidence intervals of the values of the results from the resolution phantom study (cf. Fig. 6).

To evaluate the resolution limit of the reconstructed Compton images, we used several groups of point sources with varying separation distances. In Figs. 7 and 8, the spatial resolution is shown in the cross sections from point A to point B in the reconstructed Compton images. In the Compton images reconstructed using the FBP and the MLEM algorithms, when the distances between sources were greater than 2.8 cm and 2.5 cm, re-

spectively, the sources were clearly distinguishable for both the ^{221}Fr and the ^{213}Bi Compton images. Tables 5 and 6 summarize the quantitative evaluations of the Compton images for spatial resolution. The MLEM algorithm shows the best performance.

IV. CONCLUSION

In this Monte Carlo simulation study, we evaluated the qualities of the two γ-ray DOI Compton images emitted

from the decay of the ^{225}Ac radionuclide. Based on a quantitative evaluation using various phantoms and reconstruction algorithms, we evaluated the reconstructed images for the two γ-rays and compared them. In all the simulation results, the MLEM reconstruction algorithm performed better than the FBP algorithm. At an energy of 218 keV, the precision for monitoring the ^{225}Ac radionuclide for the Compton images reconstructed using the FBP and the MLEM algorithms were limited by the fluctuation (*i.e.*, noise) caused by the increased energy uncertainty. However, because Doppler broadening and the energy uncertainty are inversely proportional to the radiation energy, both the CNR and the spatial resolution of the reconstructed images for 440 keV were better than those of the reconstructed images for 218 keV. The quantitative simulation results demonstrated the ability of the DOI Compton images to determine the position and distribution of targeted radiotherapeutic agents in TAT accurately.

REFERENCES

[1] O. Couturier *et al.*, Eur. J. Nucl. Med. Mol. Imaging **32**, 601 (2005).

[2] D. Mulford, D. Scheinberg and J. Jurcic, J. Nucl. Med. **46**, 199S (2005).

[3] Y. S. Kim and M. W. Brechbiel, Tumour Biol. **33**, 573 (2012).

[4] K. E. Baidoo, K. Yong and M. W. Brechbiel, Clin. Cancer Res. **19**, 530 (2013).

[5] M. Miederer, D. A. Scheinberg and M. R. McDevitt, Adv. Drug Deliv. Rev. **60**, 1371 (2008).

[6] M. Essler *et al.*, Eur. J. Nucl. Med. Mol. Imaging **39**, 602 (2012).

[7] R. M. deKruijff, H. T. Wolterbeek and A. G. Denkova, Pharmaceuticals **8**, 321 (2015).

[8] C. Kratochwil *et al.*, J. Nucl. Med. **57**, 1941 (2016).

[9] A. K. H. Robertson *et al.*, Phys. Med. Biol. **62**, 4406 (2017).

[10] J. D. Swart *et al.*, J. Nucl. Med. **57**, 486 (2016).

[11] J. R. Crawford *et al.*, Phys. Med. Biol. **63**, 045025 (2018).

[12] L. Han, W. L. Rogers, S. S. Huh and N. Clinthorne, Phys. Med. Biol. **53**, 7029 (2008).

[13] M. Singh and D. Doria, Med. Phys. **10**, 428 (1983).

[14] Y. F. Yang *et al.*, IEEE Trans. Nucl. Sci. **48**, 656 (2001).

[15] M-H. Richard *et al.*, IEEE Trans. Nucl. Sci. **58**, 87 (2011).

[16] M. McCleskey *et al.*, Nucl. Instrum. Meth. A **785**, 163 (2015).

[17] T. Lee, H. Lee and W. Lee, Nucl. Instrum. Meth. A **798**, 135 (2015).

[18] C. Gong *et al.*, Appl. Radiat. Isot. **124**, 62 (2017).

[19] A. Kishimoto *et al.*, Sci. Rep. **7**, 2110 (2017.)

[20] A. Koyama *et al.*, Nucl. Instrum. Meth. A **845**, 660 (2017).

[21] N. Conka Nurdan, K. Nurdan, A. B. Brill and A. H. Walenta, J. Instrum. **110**, C07018 (2015).

[22] N. Yuto *et al.*, Appl. Radiat. Isot. **139**, 238 (2018).

[23] E. Yoshida *et al.*, Nucl. Instrum. Meth. A **723**, 83 (2013).

[24] A. Kishimoto *et al.*, IEEE Trans. Nucl. Sci. **60**, 38 (2013).

[25] J. Kataoka *et al.*, Nucl. Instrum. Meth. A **732**, 403 (2013).

[26] L. C. Parra, IEEE Trans. Nucl. Sci. **47**, 1543 (2000).

[27] J. Sempau, J. M. Fernández-Varea, E. Acosta and F. Salvat, Nucl. Instrum. Meth. B **207**, 107 (2003).

[28] H. Seo *et al.*, Nucl. Instrum. Meth. A **591**, 80 (2008).

[29] T. Lee, H. Lee, Y. Kim and W. Lee, J. Korean Phys. Soc. **71**, 70 (2017).

[30] S. J. Wilderman, N. H. Clinthorne, J. A. Fessler and W. L. Rogers, Proc. IEEE Nucl. Sci. Symp. Conf. Rec. **3**, 1716 (1998).

[31] K. Lange and R. Carson, J. Comput. Assist. Tomogr. **8**, 306 (1984).